npj | microgravity

Article

Published in cooperation with the Biodesign Institute at Arizona State University, with the support of NASA

https://doi.org/10.1038/s41526-024-00444-x

Development and characterization of a low intensity vibrational system for microgravity studies

Check for updates

Omor M. Khan[1], Will Gasperini[1], Chess Necessary[2], Zach Jacobs[2], Sam Perry[2], Jason Rexroat[2], Kendall Nelson[2], Paul Gamble[2], Twyman Clements[2], Maximilien DeLeon[3], Sean Howard[1], Anamaria Zavala[1], Mary Farach-Carson[3], Elizabeth Blaber[4], Danielle Wu[3], Aykut Satici[1] ✉ & Gunes Uzer[1] ✉

Extended-duration human spaceflight necessitates a better understanding of the physiological impacts of microgravity. While the ground-based microgravity simulations identified low intensity vibration (LIV) as a possible countermeasure, how cells may respond to LIV under real microgravity remain unexplored. In this way, adaptation of LIV bioreactors for space remains limited, resulting in a significant gap in microgravity research. In this study, we introduce an LIV bioreactor designed specifically for the usage in the International Space Station. Our research covers the bioreactor's design process and evaluation of the short-term viability of cells encapsulated in hydrogel-laden 3D printed scaffolds under 0.7 g, 90 Hz LIV. An LIV bioreactor compatible with the operation requirements of space missions provides a robust platform to study cellular effects of LIV under real microgravity conditions.

In the last decade both private and public sectors have made substantial efforts to expand the boundaries of human presence beyond Earth[1–9]. In order to ensure the continued viability of long-term spaceflight, it is critical to address the physiological challenges that arise from microgravity as mission duration and reach increase[2,4,9,10]. Due to loss of gravitational loads and increased radiation, microgravity poses a unique challenge to astronaut health affecting many systems, including musculoskeletal, cardiovascular, nervous as well as excretory and reproductive systems[11,12]. In this way, microgravity affects many organs including kidneys[13] to muscles and bones, necessitating innovative solutions to mitigate these effects[10,14–17].

To combat the effects of microgravity, astronauts aboard the International Space Station (ISS) undergo rigorous exercise regimens. A recent study showed that despite 600 min/week of exercise, astronauts[18] experience continual strength deconditioning in. A major recipient of the reduced loading environment are the muscles and bones, which relies on continual mechanical input to maintain tissue homeostasis. Data from high and low volume exercise regimens show that astronauts continue to lose bone and muscle during spaceflight[19]. With longer, space missions ahead, countermeasures that may supplement exercise regimens are needed to protect musculoskeletal health.

Low-Intensity Vibration (LIV) is a low impact (<2 g where g is the Earth's gravitational field, 9.8 m/s^2) but relatively high frequency (30-500 Hz) mechanical regime developed to emulate the power spectrum of muscle contractility during exercise[20]. Application of LIV has been shown to be effective in preclinical and clinical studies. Animal studies demonstrate that LIV increases trabecular bone density and volume[21], enhance bone stiffness and strength[22], and to slow bone loss caused by disuse[23]. Further, LIV enhanced muscle contractility[24], strength[25], and cross-sectional area[26], showing that LIV signals are anabolic to skeletal muscle. Further, clinical studies support the beneficial effects of LIV in bone[27] and muscle[28–30]. Importantly, when LIV was applied in conjunction with other training regimens was beneficial to muscle activation[31]. As well, concurrent application of resistance exercise and LIV in a hind limb unloading model showed interactive effects of LIV and exercise on bone, indicating that these two modalities can be used together for a bigger benefit[32].

Cell level studies indicate that LIV increases the osteogenic differentiation in osteoblasts and mesenchymal stem cells[16,33,34] (MSCs). When applied in the context of simulated microgravity LIV not only restores MSC proliferation[35] but also restores the mechanosignaling capacity allowing cells to respond better at subsequent mechanical challenges[36]. While these studies highlight the potential benefits of LIV, there are no

[1]Department of Mechanical and Biomedical Engineering, Boise State University, Boise, ID, 83725, USA. [2]Space Tango Inc, 611 Winchester, Lexington, KY, 40505, USA. [3]Department of Bioengineering, Rice University, Houston, TX, 77005, USA. [4]Center for Biotechnology and Rd. Interdisciplinary Studies, Department of Biomedical Engineering, Rensselaer Polytechnic Institute, Troy, NY, 12180, USA. ✉e-mail: aykutsatici@boisestate.edu; gunesuzer@boisestate.edu

LIV platforms used for space applications. Deployment of such technology specifically designed for space applications, particularly those meeting the standards of the ISS are required to test the effects of LIV under real microgravity conditions.

Vibrational bioreactors intended for use in space, particularly aboard the ISS, come with unique challenges to ensure safety, reliability, and compatibility. As astronauts have limited time and must manage multiple tasks, the bioreactor should feature automated functionality to minimize astronaut time. For these needs we utilized the CubeLab 9U module (Supplementary Fig. 1), provided by Space Tango, which offers a standardized platform for microgravity experiments[2,37], allowing for a secure and controlled setting for our bioreactor. With this design selection, our design had to conform to the CubeLab Interface Control Document (ICD)[38] standards, ensuring compatibility with the ISS's operational environment. To ensure compliance with the CubeLab 9U module's requirements, our bioreactor was designed to be compact and lightweight, adhering to the CubeLab's mass limit of 19.8 lbs (9.0 kg). For the delivery of vibrational stimuli, we selected the piezoelectric actuator (P-841.30, Physik Instrumente (PI), Karlsruhe, Germany) and its closed-loop controller (E-610.S0, Physik Instrumente (PI), Karlsruhe, Germany). Additionally, the thermal environment specified by the ICD necessitates maintaining ambient temperatures around 30 degrees Celsius (°C) under active cooling. Therefore, we characterized the temperature profile of our bioreactor while inside the CubeLab without active cooling to ensure that ambient temperatures do not rise above the capabilities of the cooling equipment of the CubeLab system. Due to space constraints, bioreactor will be launched with other experiments and bioreactor operation should not affect other system due to structural vibrations or unwanted resonances. These components were tasked with providing LIV at 90 Hz with a 0.7 g peak to peak (1 g = 9.81 m/s^2) acceleration, an LIV regime selected based on previous studies demonstrating their effectiveness in promoting osteogenic differentiation under microgravity conditions[35,36]. In a precursor study within our laboratory, we developed a 3D bone analog scaffold utilizing gyroid shapes to mimic the complex architecture of bone tissue[39]. While our long-term goal is to test the effects of LIV under real microgravity conditions, for the current bioreactor design, we used these scaffolds to evaluate the media change protocols and the short-term acute toxicity of LIV delivery via our new platform.

In summary, we sought to design the first LIV bioreactor tailored to the space environment, making it a valuable tool for ongoing and future research in space biology.

Results

Linear guide selection

We first selected an appropriate linear guide to facilitate precise one-axis acceleration, crucial for the bioreactor's performance. This selection process was informed by evaluating multiple linear guides against our design criteria of consistent 1-axis LIV delivery. The vibration experiment results (Fig. 1) confirmed the Schneeberger NKL 2-95 linear guide's superior performance, with a 95.47% and 52.60% more consistent y-axis acceleration than the N preloaded prism carriage and the custom-built laboratory guide, respectively. The Schneeberger guide maintained a stable acceleration profile with lower mean values (X: 0.031 g, Y: 0.704 g, Z: 0.018 g) and standard deviations (X: ±0.000 g, Y: ±0.005 g, Z: ±0.006 g), indicating its precise control over vibrational input. The Schneeberger NKL 2-95 guide also exhibited the lowest Coefficient of Variation (CV) in the Y-axis (0.71%), confirming its better consistency in performance compared to the N preloaded prism carriage (5.07%) and the custom-built laboratory guide (1.61%). In comparison, the N preloaded prism carriage showed higher variability, particularly in the x-axis (0.473 g ± 0.024) and z-axis (0.133 g ± 0.008), while the laboratory guide using Misumi roller guides presented intermediate stability (X: 0.089 g ± 0.007, Y: 0.684 g ± 0.011, Z: 0.071 g ± 0.000). All guides met the experimental requirement of 0.7 g peak to peak acceleration in the y-axis, demonstrating their adequacy for the intended vibrational studies.

Thermal Profile in the Cubelab Environment

We conducted a thermal analysis to ensure that the bioreactor operation stayed within operational parameter of the CubeLab 9U system. The temperature profile (Fig. 2) of the CubeLab environment was recorded in both "Open" and "Enclosed" states to see what effect the enclosure had during the 25-min LIV period. Temperature data were recorded every second from

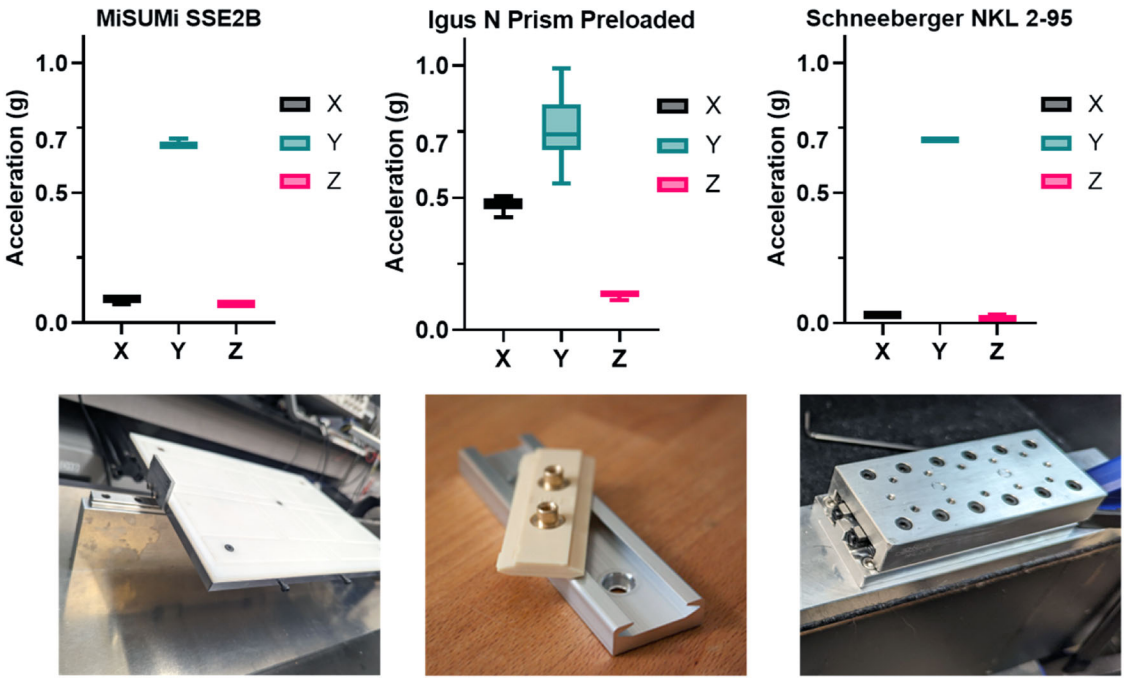

Fig. 1 | Comparison of peak-to-peak accelerations for three different linear guides under 90 Hz, 0.7 g peak-to-peak vibration. The guides tested were an N-Prism linear guide, a Schneeberger linear guide, and a Misumi linear guide. Box and violin plots represent the distribution of peak-to-peak accelerations in the X, Y, and Z axes over a 20-min test period. The Schneeberger guide demonstrated the most consistent performance, with a peak-to-peak acceleration of 0.7 g in the Y-axis and minimal vibration translation to the X and Z axes.

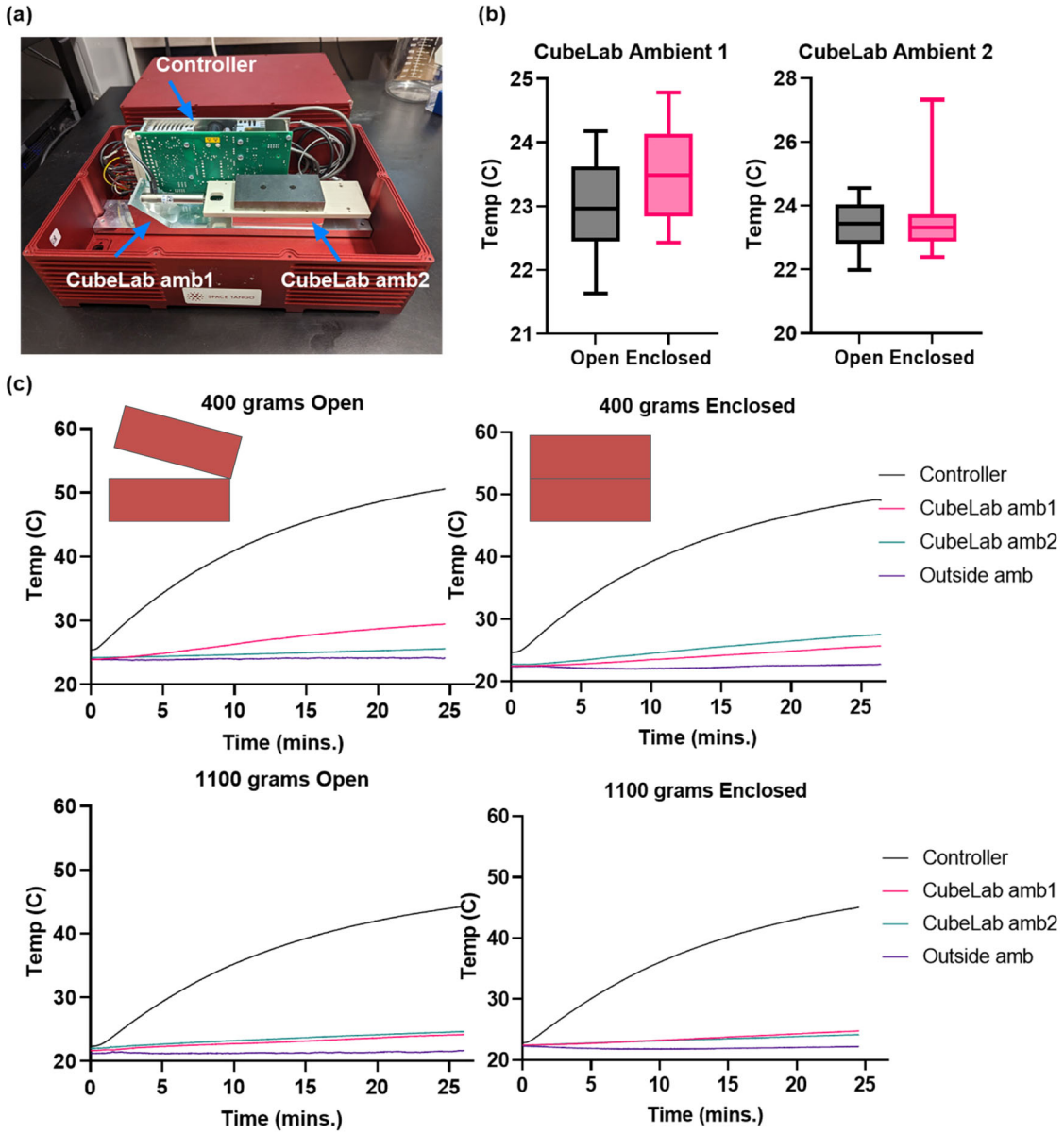

Fig. 2 | Differential heating effects on the vibrational bioreactor and surrounding environment. a Photograph of the CubeLab in the open configuration, highlighting the vibrational actuator, controller, Schneeberger NKL 2-95 slide, and the base holding the bioreactor. Arrows indicate the the placement of thermocouples at CubeLab ambient 1(CubeLab amb1) and CubeLab ambient 2 (CubeLab amb2). **b** Box plots comparing ambient temperatures at CubeLab amb1 and amb2 for open and enclosed conditions, illustrating the impact of the CubeLab's cover on internal temperature stability. **c** Time-temperature plots showing the temperature profiles over 25 min for 400 g and 1100 g payloads under both open and enclosed conditions. Despite significant heat generation from the controller, ambient temperatures remain within safe range for cell viability.

three locations, ambient 1, ambient 2 and controller as indicated in Fig. 1a. Ambient 1 and Ambient 2 temperatures were compared between Enclosed and Open conditions (Fig. 1b). For these tests, we pooled the date from two different payloads (400 and 1100 g), to simulate the expected operational weight range (Fig. 1c).

A paired t-test analysis revealed a significant difference in the temperature profiles between the "Open" and "Enclosed" configurations. For ambient 1, the results showed a small increase in temperature when the CubeLab was enclosed, with a mean difference of 0.59 °C between the two conditions ($p < 0.0001$). Despite this increase, the temperatures remained stable, with ambient 1 averaging 23 ± 0.72 °C in the "Open" configuration and 25 ± 0.65 °C in the "Enclosed" configuration.

Similarly, for ambient 2, the paired t-test indicated a statistically significant difference between the "Open" and "Enclosed" conditions ($p < 0.0001$), though the mean difference was smaller at −0.065 °C. In the "Open" configuration, ambient 2 stabilized at 24 ± 0.60 °C, while in the "Enclosed" configuration, it reached 26 ± 0.58 °C. Importantly, even in the "Enclosed" configuration, the temperatures remained within acceptable limits, suggesting that passive heat dissipation mechanisms were sufficient to maintain a safe operational environment for the duration of the experiments. No changes in controller temperature was found.

Vibration characterization

We next conducted a vibrational analysis of the bioreactor's behavior using both COMSOL simulations and experimental testing to ensure that the applied vibrations were within the operational parameters. Experimental characterization of the bioreactor's vibrational dynamics, supplemented by COMSOL simulations, confirmed operational stability across the frequency spectrum. The simulations indicated no resonant frequencies within the operational range, with the first mode of vibration occurring at 929 Hz

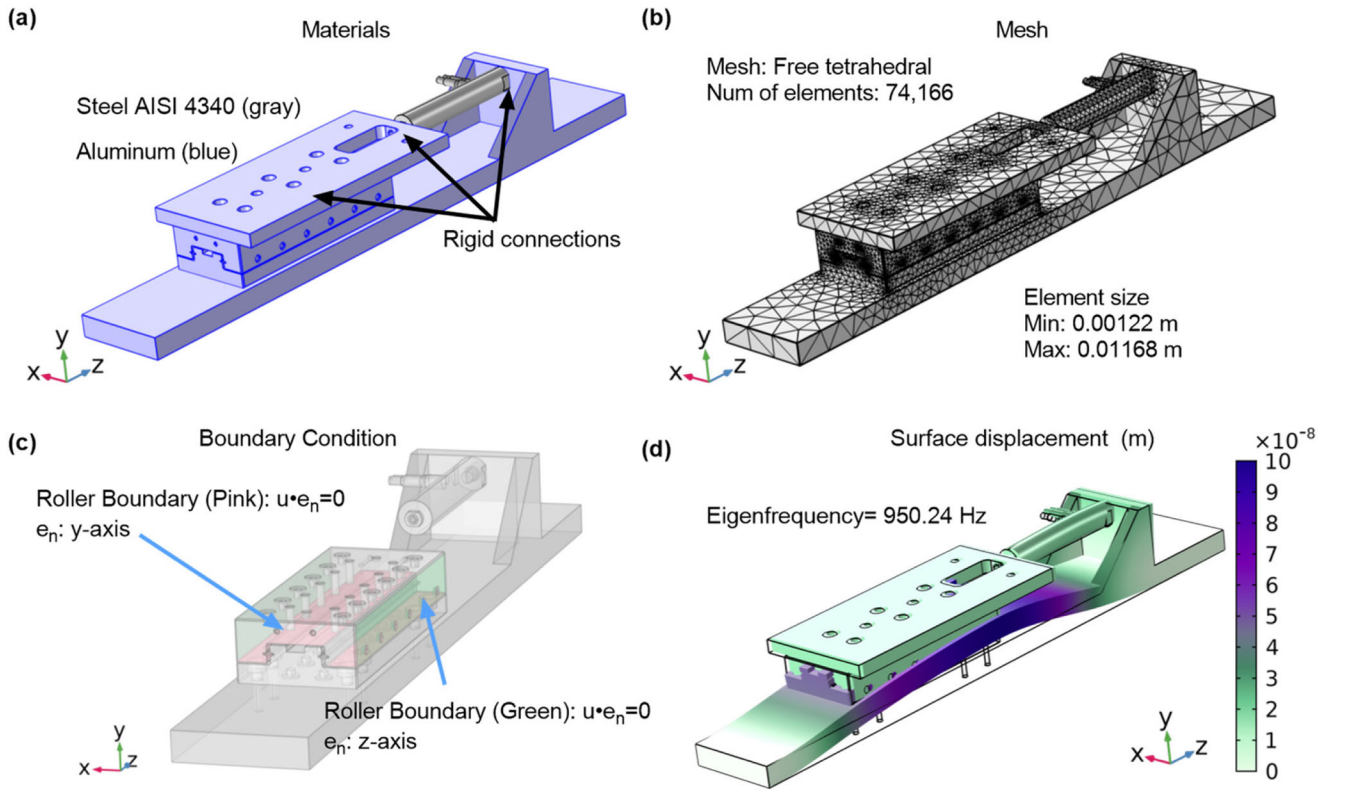

Fig. 3 | Vibrational analysis of the bioreactor using COMSOL Multiphysics. a The bioreactor assembly with components materials assigned. **b** The applied mesh ensuring resolution for accurate mode shape determination. **c** Roller boundary conditions are applied to simulate linear guide constraints. **d** The first mode shape at 950.24 Hz, demonstrating primary deformation.

Table 1 | Acceleration ratio in each non-targeted axes to the acceleration of target direction, highlighting the relative distribution of vibrational energy across all axes

Frequency (Hz)	X/Y	Z/Y
60	0.06	0.06
70	0.06	0.13
80	0.06	0.13
85	0.06	0.13
90	0.06	0.13
95	0.06	0.10
110	0.06	0.13
130	0.06	0.13
150	0.06	0.10
200	0.13	0.16
250	0.13	0.16
300	0.13	0.19
500	0.14	0.19

The bioreactor was subjected to vibration of 0.3 g peak-to-peak across the entire 60 Hz to 500 Hz frequency range. Error analysis was not performed for this characterization study as it focuses on the vibration characterization rather than statistical variability.

Table 2 | Acceleration ratio in each non-targeted axes to the acceleration of target direction, highlighting the relative distribution of vibrational energy across all axes

Frequency (Hz)	X/Y	Z/Y
80	0.06	0.09
85	0.06	0.09
90	0.06	0.09
95	0.055	0.09
110	0.07	0.09
130	0.09	0.09
150	0.06	0.10

The bioreactor was subjected to vibration of 0.7 g peak-to-peak limited to frequencies between 80 Hz and 150 Hz due to system constraints.

(Fig. 3), thus minimizing the risk of resonance interference. Experimental tests validated the simulation, demonstrating effective vibrational isolation at operational frequencies, with X/Y and Z/Y acceleration ratios remaining below 0.13 frequencies lower than 300 Hz. As frequency increased, a corresponding rise in these ratios was observed, suggesting higher transference of vibration to non-targeted axes. Tables 1 and 2 encapsulates these findings.

Cell viability in scaffold-hydrogels

To validate the bioreactor's compatibility with cellular studies, we performed tetrazolium salt (XTT) and Live/Dead assays to confirm that the bioreactor design did not adversely affect short-term cell viability. The XTT assay results indicated no significant difference in metabolic activity between the vibrated (+LIV) ($p = 0.9973$) and non-vibrated (-LIV) ($p > 0.9999$) samples from day 1 (D1) to day 4 (D4) showing no adverse effects of LIV on the cell viability. For a more direct observation of cell viability, Live/Dead imaging was employed. The imaging results, presented in Fig. 4c-f and (Supplementary Fig. 6), visually demonstrate the proportion of live (green) to dead (red) cells, providing a qualitative assessment that LIV does not increase cell death.

Diffusion Study

Diffusion of nutrients are critical for cell viability[40]. Our current CubeWell design holds 8 mL of media. Since media change happens by pushing new

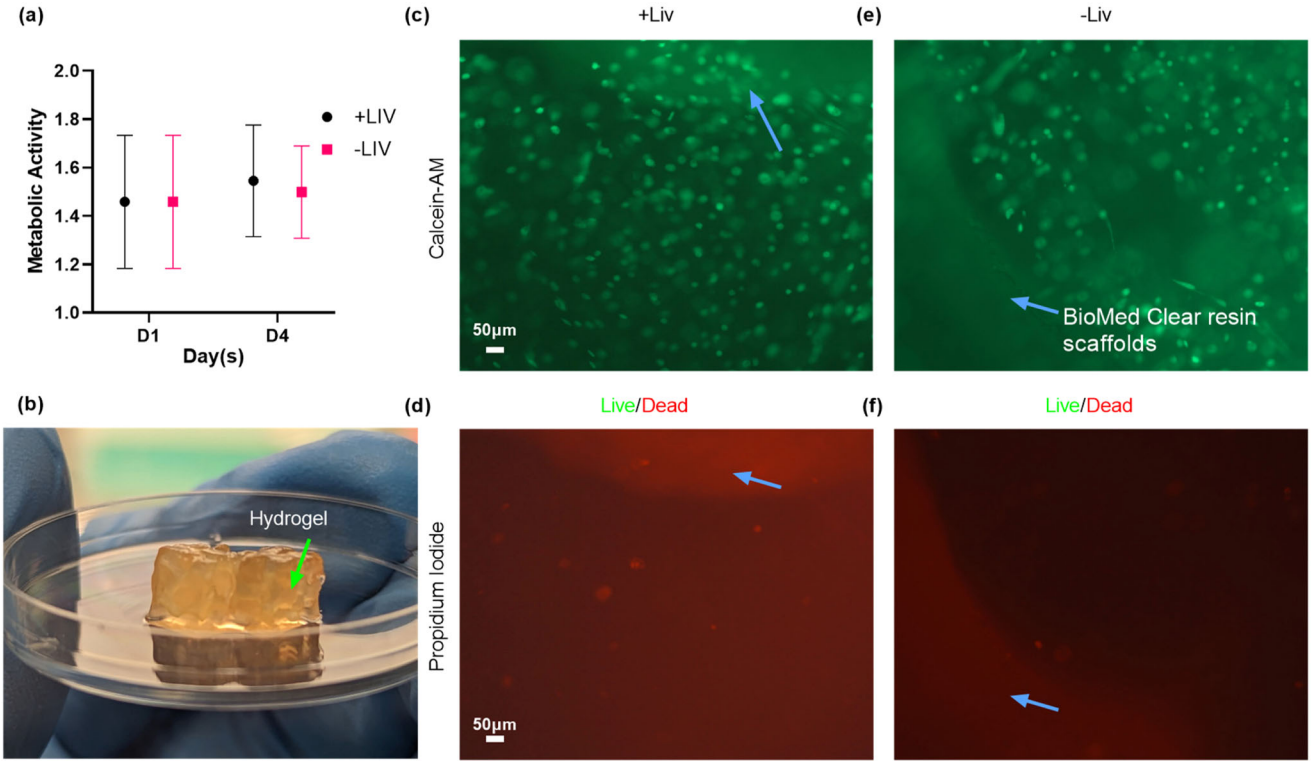

Fig. 4 | Analysis of stem cell viability and metabolic activity in SLA-printed scaffolds. This figure presents the results of a 4-day experiment investigating the survival and metabolic activity of stem cells grown in SLA-printed scaffolds (blue arrows). **a** Metabolic activity was measured using an XTT assay at day 1 (mean = 1.4, SD = 0.23) and at day 4 (mean = 1.5, SD = 0.19), showing a slight increase over time despite high standard deviations due to a small sample size (n = 4 per group). Analysis showed no significance between groups and days. Concurrently, (**c**–**f**) Live/Dead staining and imaging highlighted a predominance of viable (green) cells over dead ones (red), reinforcing the potential for successful cell growth within these scaffolds.

media into the chamber, 100% media change cannot be achieved without pumping more than 8 mL media. This is not ideal due to weight and volume limitations of the CubeLab system. For this reason our media change protocol was set to a 60% media change (5 mL) followed by a recirculation protocol to ensure adequate nutrient diffusion. Therefore, we quantified the media exchange within the CubeWells via COMSOL simulations and experiments.

The diffusion characteristics within the CubeWells (Supplementary Fig. 7) were initially modeled using COMSOL simulations to establish an efficient media exchange protocol. According to the simulations illustrated in Fig. 5b and c, it was seen that by employing a pumping rate of 1 mL/min, approximately 80% of the volume of CubeWell would be occupied by fresh media during a span of 3 min. This rate of media replacement would result in new media reaching to entire well by the 5-min mark. These findings informed the operational parameters for the media pump in subsequent in-vitro validation experiments. Our media change parameters exert minimal fluid shear, using 1 mL/min fluid flow rate we estimated fluid shear around samples to be less than 0.1 dyn/cm^2 (0.01 Pa). Osteocytes are mechanosensitive cells that respond to fluid shear stress as low as 0.5Pa[41]. As our fluid shear was at least an order of magnitude lower, we assumed no effect.

In practice, the diffusion regime for the in-vitro experiment, visualized in Fig. 5a, involved a 5-min media pumping phase at the same flow rate, followed by a 15-min recirculation period. The high-speed camera monitoring revealed a consistent media distribution pattern (Fig. 5d, e), with a notable 55-second delay in reaching the center, bottom-left, and bottom-right locations compared to the simulation. Despite this delay, at the end of recirculation, all the samples received adequate fresh media.

Discussion

The selection of the linear guide was critical for the bioreactor's performance. Our results indicated that the Schneeberger NKL 2-95 linear guide provided consistent one-axis acceleration, crucial for minimizing disturbances during vibration. Thermal characterization within the CubeLab environment demonstrated that the system could sustain a stable temperature profile, with variations within ±0.80 °C over a 25-min operational period. This indicates that the bioreactor's thermal management is adequate for the tested operational conditions. The simulations provided theoretical assurance that the bioreactor's design avoids resonant frequencies within the operational range, with the first resonant mode predicted at 929 Hz and experimentally measured ratio of non-targeted to targeted axis accelerations remained below 15% under 300 Hz suggesting that targeted operation frequency of 90 Hz was safe. We also confirmed that LIV did not adversely affected cell viability during a 4-day period. Finally, we confirmed that automated media change protocol resulted in uniform cell nourishment.

In conclusion, this study presented and tested performance of a new LIV bioreactor designed for ISS studies. The research focused on validating the bioreactor's mechanical and biological performance, ensuring its compatibility with the unique requirements of space missions. We expect that this bioreactor would provide a robust platform to study effects of LIV under real microgravity conditions.

Methods

Experimental setup of the LIV bioreactor

A custom amplifier circuit was designed with a Sallen-Key[42] second-order lowpass filter topology (Supplementary Fig. 2). The filter was tuned to isolate a 90 Hz sine wave from a modulated PWM signal, removing the extraneous frequencies. This process produced a clean sine wave to drive the piezoelectric actuator, providing the precise vibrational stimulus required for the biological experiments.

For all the characterization tests of the vibration bioreactor, a standard laboratory signal generator was used to deliver the input signals. The

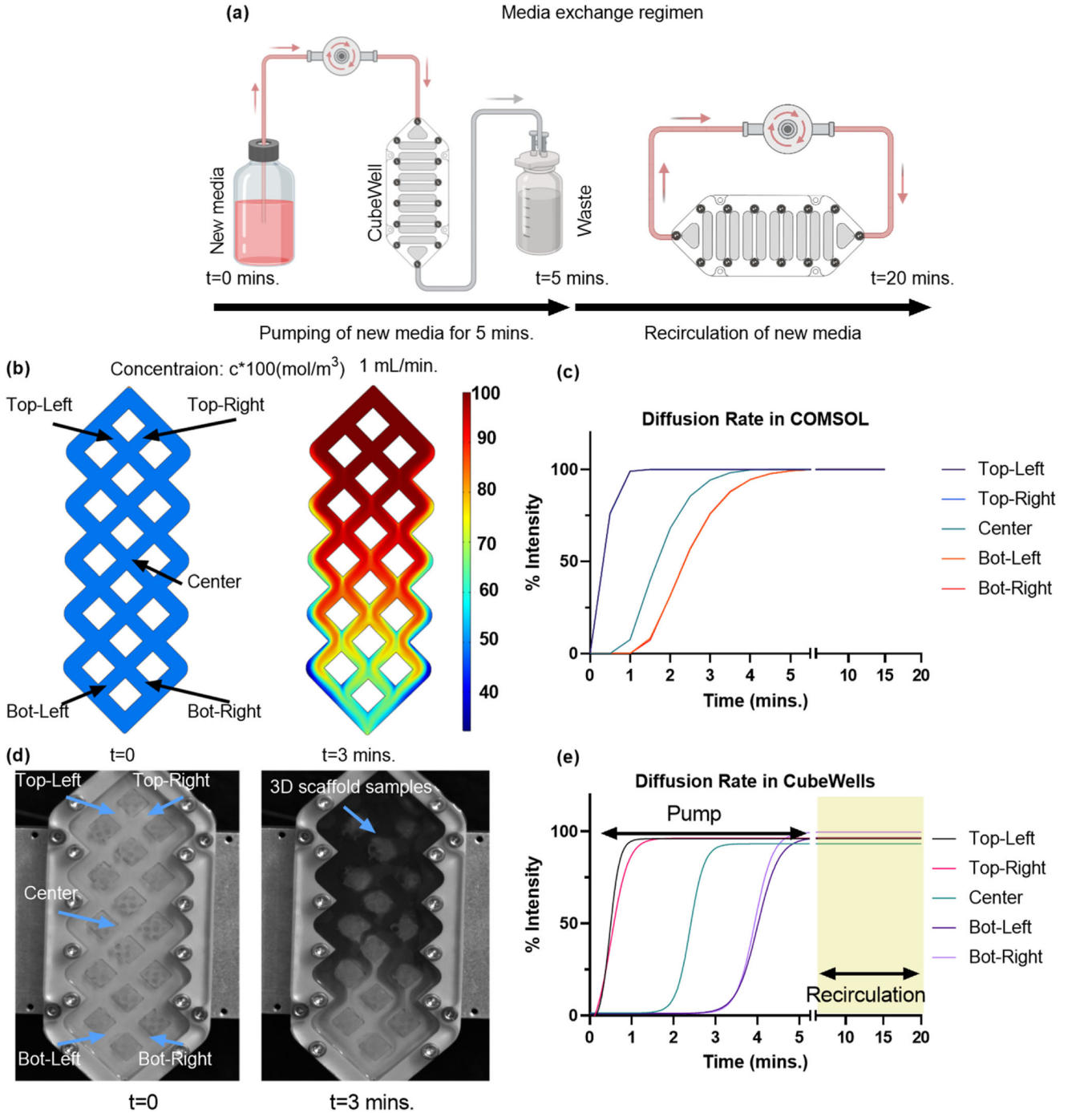

Fig. 5 | Diffusion study of custom well plate for cell culture. a For most efficient volume change, a 5-min pump followed by a 15 min. recirculation is implemented in the media change regimen for the real experiment. **b** COMSOL simulation depicting media concentration profile and its (**c**) quantitative analysis. Note: Only three curves are visible due to the overlap of the top left and top right, as well as the bottom left and bottom right curves, which exhibit identical diffusion dynamics. **d** Real experiment replicating the COMSOL simulation using dye as new media for visualization and (**e**) intensity values of the real experiment showcasing the concentration gradient within the 5 min. pump and 15 min. recirculation in highlighted region.

developed signal source was specifically utilized during the payload verification test (PVT) at Space Tango to ensure its functionality under operational conditions. All testing was conducted in a closed-loop control configuration where the actuator was strain-controlled. In this setup, the controller maintained the vibration at the specified voltage input from the signal source, rather than directly controlling for acceleration conditions. This approach allowed the actuator to consistently follow the input signal, delivering precise vibrational stimuli according to the designed strain parameters.

Linear guide selection

To select a linear guide capable of delivering precise one-axis acceleration, we conducted performance evaluations on three different models. Using LabVIEW software, we measured the acceleration profiles of each guide with a MEMSIC CXL04GP3 accelerometer (Supplementary Fig. 3). The guides were tested for their ability to sustain a 0.7 g peak-to-peak acceleration at a frequency of 90 Hz over a 20-min duration. The objective was to identify a guide that would restrict vibrations to the intended axis, ensuring accurate delivery of mechanical stimuli to the samples. The tested guides

(Fig. 1) included: a custom-built roller-based guide (SS2EB, Misumi, Schaumburg, IL), known for smooth motion; a low-maintenance plastic linear guide (N Prism Preloaded, Igus Inc., Rumford, RI); and a Schneeberger roller-based linear guide (NKL 2-95, Schneeberger Inc., Woburn, MA).

Thermal characterization of the LIV bioreactor

The thermal performance of the LIV bioreactor was evaluated to determine its suitability for sustaining biological experiments within the CubeLab module. The fully assembled bioreactor, including the piezoelectric actuator, closed-loop controller, and the selected linear guide-Schneeberger NKL 2-95, was installed inside the CubeLab. Thermocouples (Type K) were positioned: directly inside the controller housing, above the actuator, adjacent to the biological sample area, and within the external ambient environment of the CubeLab (Fig. 2 and Supplementary Fig. 4).

LabVIEW software with the NI 9211 DAQ card (National Instruments, Austin, TX, USA) was utilized for both control of the vibrational input and data acquisition of the thermal output. The system was tested with two different payload conditions, 400 grams and 1100 grams, to simulate varying experimental loads. The operational test consisted of a 25-min vibration cycle at 0.7 g peak-to-peak acceleration and a frequency of 90 Hz.

Thermal characterization was conducted under two distinct CubeLab configurations: an "Open" setup with the top cover removed and an "Enclosed" setup where the module was entirely sealed. These tests were performed without the integration of active cooling systems to assess the bioreactor's inherent thermal management capabilities under operational conditions. Data collected during these tests were analyzed to understand the thermal dynamics of the system, with particular attention to the temperature stability and heat dissipation efficiency in both "Open" and "Enclosed" states.

Determination of vibration characteristics of the bioreactor

The vibrational characteristics of our bioreactor were analyzed through both simulation and experimental testing. In the simulation phase, COMSOL was used to study the system's dynamics. A detailed CAD model of the bioreactor, which included the base, actuator, linear guide, and payload holder, was integrated into the simulation environment. Notably, for simplification and a conservative approach in our analysis, the material for the piezoelectric actuator was assumed to be the same as its housing—standard stainless steel. This assumption allowed us to focus on the primary vibration modes crucial for the bioreactor's functionality in microgravity, without the complexities of modeling the piezoelectric properties.

A mesh convergence study was conducted to ensure the accuracy of the simulation results. The fine mesh configuration used in the manuscript consisted of 74,166 elements with a maximum element size of 0.0168, yielding a first eigenfrequency of 950.24 Hz. To verify the reliability of this mesh, a finer mesh consisting of 212,917 elements was also tested, resulting in a first eigenfrequency of 944.75 Hz. The minimal difference between these results (less than 1%) confirmed that the fine mesh was sufficient for capturing the key vibrational dynamics, providing a good balance between computational efficiency and accuracy.

This setup, which mirrored real-world constraints and was executed with a standard mesh configuration, provided a robust and efficient method to assess the vibrational dynamics of the bioreactor.

Concurrently, experimental tests were conducted to validate the simulation results and further understand the bioreactor's vibrational behavior. The system was subjected to vibrations at a targeted 0.4 g peak-to-peak acceleration across a frequency range of 50–500 Hz, with finer increments around the critical 90 Hz range. Subsequent tests aimed for a 0.7 g peak-to-peak vibration; however, due to the actuator's constraints, only at frequencies from 80 Hz to 150 Hz. Results were presented in Tables 1 and 2.

Determination of short-term scaffold viability

Cell viability on stereolithography (SLA)-printed scaffolds made from Formlabs BioMed Clear resin was assessed using XTT assays for quantitative analysis and Live/Dead imaging for qualitative evaluation. The resin was selected for its precision in creating complex structures. Scaffolds were integrated within a hydrogel to improve the biomimetic quality for cell culture studies. The study employed both vibrated and non-vibrated samples as experimental and control groups (+LIV/−LIV), respectively. Each week's samples (n = 4/week for 2 weeks) were biological replicates, with fresh samples prepared for the subsequent week following the identical protocol as the initial week.

In order to prepare the scaffolds, murine mesenchymal stem cells (MSCs) were encapsulated within a hydrogel[43] composed of Thiolated Hyaluronic Acid (HA) (Advanced Biomatrix, #GS22F), functionalized with specific amino sequences: PQ (GGGPQ ↓ IWGQGK concentrated at 44.973 mgs/mL) and RGD (GRGDS concentrated at 73.7mgs/mL) with a volume ratio of 4 HA:1 RGD: 1PQ. The encapsulated cells then were seeded into hydrogels containing gyroid-shaped scaffolds as previoulsy reported[39]. Scaffolds were generated using 25% bone volume, corresponding to bone volumes of 8 week old male C57BL/6 J mice[44]. Gyroid geometries representing trabecular structures were generated using the equation: $\sin(x)\cos(y) + \sin(y)\cos(z) + \sin(z)\cos(x) < t$, where t is a constant linearly related to the percent volumes[45]. For 25%, the t scaling value used was −0.752. Scaffold models were generated using *MathMod v8.0* and scaled to final dimensions of 5 mm x 5 mm x 5 mm. These scaffolds were fabricated using the BioMed Clear resin and were SLA printed using a Form 2 printer (Supplementary Fig. 5).

Post-seeding, the scaffold-hydrogels were transferred to a 96-well plate containing the osteogenic media (α-MEM, supplemented with 10% FBS (v/v), 100 U/mL penicillin, 100 µg/mL streptomycin, 50ug/ml Ascorbic Acid, and 10 mM beta-glycerophosphate). The entire setup then was placed in an incubator. A distinct vibration regime was implemented, wherein the samples were subjected to a consistent vibration of 0.7 g peak-to-peak at 90 Hz for 20 min. This vibration was administered twice daily, with a 2-h interval between each session.

On the first and fourth day, an XTT assay was performed to assess cell viability. The assay utilized two primary reagents: an electron mediator solution and the XTT developer reagent (Cayman Chemical, #10010200). Following the manufacturer's protocol, the samples were incubated for approximately 2 h at 37 °C. The absorbance of the assay wells then was measured using a microtiter plate reader, capturing values between 400 and 500 nm wavelengths.

On the fifth day, live/dead imaging was conducted. The cells were stained using Calcein AM (green) to identify live cells, Propidium Iodide (red) to mark dead cells, and Hoechst 33342 (blue) for nuclear staining according to the manufacturer's specifications (EMD Millipore #CBA415). The stained samples were visualized under a fluorescence microscope. While no quantitative data was extracted from these images, they provided a visual representation of the ratio between live and dead cells, offering insights into cell health and viability.

Diffusion dynamics within the CubeWells

To ensure consistent cell culture conditions within the custom-designed CubeWells by Space Tango, a diffusion study was conducted. Initial tests verified the CubeWells' structural integrity through a visual leak assessment. Here we evaluated the efficiency of a miniaturized pump in introducing new media into the CubeWell and to confirm uniform media distribution across the well. This was achieved through both COMSOL simulations and real-time camera observations.

To predict the diffusion dynamics within the custom-designed CubeWell system, a multiphysics simulation was conducted using COMSOL. The study combined two primary modules: Laminar Flow and Transport of Diluted Species. The Laminar Flow module was employed to simulate the fluid flow into the CubeWell, while the Transport of Diluted Species module was used to visualize the influx of new media, set at a concentration of 1 mol/m^3. The simulation was constrained by defining the inlet at the top and outlet at the bottom of the CubeWell (Fig. 5b), along with the boundary walls, ensuring a realistic representation of the media exchange process.

For experimental validation of the COMSOL, the CubeWells were pre-filled with 8 mL of water. Within this environment, SLA-printed scaffolds made from BioMed Clear resin were introduced. These scaffolds, measuring 5x5x5mm, were encapsulated in hydrogels (Fig. 4b), mimicking the cellular constructs intended for subsequent cell culture experiments. To simulate the introduction of fresh media, a mixture of water and Royal Blue Icing color dye (Wilton, #17111150) was prepared. This simulated medium then pumped into the CubeWell at a consistent rate of 1 mL/min. The entire process of media exchange, including the diffusion of the dye and fluid movement within the CubeWells, was captured using a high-speed camera (Photron FASTCAM MINI UX50) set at 1000 fps. This recording spanned a duration of 5 min, providing a detailed visual account of the diffusion dynamics. Post-recording, the captured footage was analyzed to quantify diffusion within the CubeWell system. Five distinct locations within the CubeWell were selected for this analysis. At these points, the intensity values of the dye were measured over time, offering a quantitative perspective on the diffusion rates and patterns.

Data availability

The datasets used and/or analyzed during the current study are available from the corresponding author on reasonable request.

Received: 18 March 2024; Accepted: 24 October 2024;
Published online: 20 November 2024

References

1. Shiba, D. et al. Development of new experimental platform 'MARS'—Multiple Artificial-gravity Research System—to elucidate the impacts of micro/partial gravity on mice. *Sci. Rep.* **7**, 10837 (2017).
2. Poghosyan, A. & Golkar, A. CubeSat evolution: Analyzing CubeSat capabilities for conducting science missions. *Prog. Aerosp. Sci.* **88**, 59–83 (2017).
3. Lumpp, J. E., Erb, D. M., Clements, T. S., Rexroat, J. T. & Johnson, M. D. The CubeLab Standard for improved access to the International Space Station. in *2011 Aerospace Conference* 1–6 (2011). https://doi.org/10.1109/AERO.2011.5747232.
4. Garzaniti, N., Tekic, Z., Kukolj, D. & Golkar, A. Review of technology trends in new space missions using a patent analytics approach. *Prog. Aerosp. Sci.* **125**, 100727 (2021).
5. Gao, Z. Development and the state-of-art facility for aerospace vehicle. *Highlights Sci. Eng. Technol.* **38**, 251–257 (2023).
6. Ficca, A., Marulo, F. & Sollo, A. An open thinking for a vision on sustainable green aviation. *Prog. Aerosp. Sci.* **141**, 100928 (2023).
7. Bozdoğan, R., Kotil, T. & Öztürk, F. Technological Development of Turkish Aerospace. in *National Technology Initiative: Social Reflections and Türkiye's Future* (ed. Kacır, M. F.) 475–494 (Türkiye Bilimler Akademisi Yayınları, 2022). https://doi.org/10.53478/TUBA.978-625-8352-17-7.ch25.
8. Adler, E. J. & Martins, J. R. R. A. Hydrogen-powered aircraft: Fundamental concepts, key technologies, and environmental impacts. *Prog. Aerosp. Sci.* **141**, 100922 (2023).
9. Gibney, E. European space windfall will fast-track science missions. *Nature* (2019) https://doi.org/10.1038/d41586-019-03707-w.
10. Stavnichuk, M., Mikolajewicz, N., Corlett, T., Morris, M. & Komarova, S. V. A systematic review and meta-analysis of bone loss in space travelers. *Npj Microgravity* **6**, 13 (2020).
11. Tomsia, M. et al. Long-term space missions' effects on the human organism: what we do know and what requires further research. *Front. Physiol.* **15**, 1284644 (2024).
12. Krittanawong, C. et al. Human health during space travel: state-of-the-art review. *Cells* **12**, 40 (2022).
13. Siew, K. et al. Cosmic kidney disease: an integrated pan-omic, physiological and morphological study into spaceflight-induced renal dysfunction. *Nat. Commun.* **15**, 4923 (2024).
14. Smith, S. M. et al. Bone metabolism and renal stone risk during International Space Station missions. *Bone* **81**, 712–720 (2015).
15. The impact of microgravity on bone in humans. *Bone* **87**, 44–56 (2016).
16. Zhang, C. et al. Effects of mechanical vibration on proliferation and osteogenic differentiation of human periodontal ligament stem cells. *Arch. Oral. Biol.* **57**, 1395–1407 (2012).
17. Juhl, O. J. et al. Update on the effects of microgravity on the musculoskeletal system. *Npj Microgravity* **7**, 1–15 (2021).
18. Scott, J. M. et al. Effects of exercise countermeasures on multisystem function in long duration spaceflight astronauts. *Npj Microgravity* **9**, 11 (2023).
19. English, K. L. et al. High intensity training during spaceflight: results from the NASA Sprint Study. *Npj Microgravity* **6**, 1–9 (2020).
20. Huang, R. P., Rubin, C. T. & McLeod, K. J. Changes in postural muscle dynamics as a function of age. *J. Gerontol. A. Biol. Sci. Med. Sci.* **54**, B352–B357 (1999).
21. Rubin, C., Turner, A. S., Bain, S., Mallinckrodt, C. & McLeod, K. Low mechanical signals strengthen long bones. *Nature* **412**, 603–604 (2001).
22. Rubin, C. et al. Quantity and quality of trabecular bone in the femur are enhanced by a strongly anabolic, noninvasive mechanical intervention. *J. Bone Miner. Res* **17**, 349–357 (2002).
23. Rubin, C., Xu, G. & Judex, S. The anabolic activity of bone tissue, suppressed by disuse, is normalized by brief exposure to extremely low-magnitude mechanical stimuli. *FASEB J. Publ. Fed. Am. Soc. Exp. Biol.* **15**, 2225–2229 (2001).
24. McKeehen, J. N. et al. Adaptations of mouse skeletal muscle to low-intensity vibration training. *Med. Sci. Sports Exerc.* **45**, 1051–1059 (2013).
25. Mettlach, G. et al. Enhancement of neuromuscular dynamics and strength behavior using extremely low magnitude mechanical signals in mice. *J. Biomech.* **47**, 162–167 (2014).
26. Xie, L., Rubin, C. & Judex, S. Enhancement of the adolescent murine musculoskeletal system using low-level mechanical vibrations. *J. Appl. Physiol. Bethesda Md 1985* **104**, 1056–1062 (2008).
27. Marín-Cascales, E. et al. Whole-body vibration training and bone health in postmenopausal women: A systematic review and meta-analysis. *Med. (Baltim.)* **97**, e11918 (2018).
28. Gilsanz, V. et al. Low-level, high-frequency mechanical signals enhance musculoskeletal development of young women with low BMD. *J. Bone Miner. Res.* **21**, 1464–1474 (2006).
29. Blottner, D. et al. Human skeletal muscle structure and function preserved by vibration muscle exercise following 55 days of bed rest. *Eur. J. Appl. Physiol.* **97**, 261–271 (2006).
30. Muir, J., Kiel, D. P. & Rubin, C. T. Safety and severity of accelerations delivered from whole body vibration exercise devices to standing adults. *J. Sci. Med. Sport* **16**, 526–531 (2013).
31. Liu, Y., Fan, Y. & Chen, X. Effects of whole-body vibration training in static and dynamic semi-squat patterns on the lower limb muscle activity. *Sci. Rep.* **13**, 14432 (2023).
32. Li, Z. et al. Whole-body vibration and resistance exercise prevent long-term hindlimb unloading-induced bone loss: independent and interactive effects. *Eur. J. Appl. Physiol.* **112**, 3743–3753 (2012).
33. Tirkkonen, L. et al. The effects of vibration loading on adipose stem cell number, viability and differentiation towards bone-forming cells. *J. R. Soc. Interface* **8**, 1736–1747 (2011).
34. Pongkitwitoon, S., Uzer, G., Rubin, J. & Judex, S. Cytoskeletal configuration modulates mechanically induced changes in mesenchymal stem cell osteogenesis, morphology, and stiffness. *Sci. Rep.* **6**, 34791 (2016).
35. Touchstone, H. et al. Recovery of stem cell proliferation by low intensity vibration under simulated microgravity requires LINC complex. *Npj Microgravity* **5**, 1–9 (2019).

36. Thompson, M., Woods, K., Newberg, J., Oxford, J. T. & Uzer, G. Low-intensity vibration restores nuclear YAP levels and acute YAP nuclear shuttling in mesenchymal stem cells subjected to simulated microgravity. *Npj Microgravity* **6**, 1–11 (2020).
37. Jacobs, Z., Rawashdeh, S. & Lumpp, J. A SPA-1 Enabled Plug-and-Play CubeLab for ISS Payloads. in *Infotech@Aerospace 2012* (American Institute of Aeronautics and Astronautics, Garden Grove, California, 2012). https://doi.org/10.2514/6.2012-2507.
38. CubeLab-Interface-Control_Document-Rev2-1.pdf. https://ueberflieger.space/wp-content/uploads/2021/08/CubeLab-Interface-Control_Document-Rev2-1.pdf.
39. Regner, A. M. et al. Increased deformations are dispensable for cell mechanoresponse in engineered bone analogs mimicking aging bone marrow. 2023.09.24.559187 Preprint at https://doi.org/10.1101/2023.09.24.559187 (2023).
40. Hubka, K. M., Carson, D. D., Harrington, D. A. & Farach-Carson, M. C. Perlecan domain I gradients establish stable biomimetic heparin binding growth factor gradients for cell migration in hydrogels. *Acta Biomater.* **97**, 385–398 (2019).
41. Kleinnulend, J., Semeins, C. M., Ajubi, N. E., Nijweide, P. J. & Burger, E. H. Pulsating fluid flow increases nitric oxide (NO) synthesis by osteocytes but not periosteal fibroblasts - correlation with prostaglandin upregulation. *Biochem. Biophys. Res. Commun.* **217**, 640–648 (1995).
42. Zumbahlen, H. CHAPTER 8 - Analog Filters. in *Linear Circuit Design Handbook* (ed. Zumbahlen, H.) 581–679 (Newnes, Burlington, 2008). https://doi.org/10.1016/B978-0-7506-8703-4.00008-0.
43. Sablatura, L. K., Tellman, T. V., Kim, A. & Farach-Carson, M. C. Bone marrow endothelial cells increase prostate cancer cell apoptosis in 3D triculture model of reactive stroma. *Biology* **11**, 1271 (2022).
44. Papageorgiou, M., Föger-Samwald, U., Wahl, K., Kerschan-Schindl, K. & Pietschmann, P. Age- and strain-related differences in bone microstructure and body composition during development in inbred male mouse strains. *Calcif. Tissue Int.* **106**, 431–443 (2020).
45. Rammohan, A. V. & Tan, V. B. C. Morphological models of trabecular bone suitable for high-porosity regions and vertebrae. *Comput. Methods Biomech. Biomed. Engin.* **19**, 1418–1422 (2016).

Acknowledgements

This study was supported by, AG059923, NSF1929188 and, NSF 2025505.

Author contributions

Omor Khan: concept/design, data analysis/interpretation, manuscript writing, Will Gasperini: concept/design, data analysis/interpretation, Chess Necessary: concept/design, Zach Jacobs: concept/design, Sam Perry: concept/design, Jason Rexroat: concept/design, Maximilien DeLeon: concept/design, data analysis/interpretation, manuscript writing, Kendall Nelson: concept/design, data analysis/interpretation, Paul Gamble: concept/design, final approval of manuscript, Twyman Clements: concept/design, final approval of manuscript, Anamaria Zavala: data analysis, concept/design, final approval of manuscript, Sean Howard: data analysis, concept/design, final approval of manuscript, Mary Farach-Carson: data analysis, concept/design, Elizabeth Blaber: data analysis, concept/design, Danielle Wu: data analysis, concept/design, Aykut Satici: concept/design, data analysis/interpretation, financial support, manuscript writing, final approval of manuscript, Gunes Uzer: concept/design, data analysis/interpretation, financial support, manuscript writing, final approval of manuscript

Competing interests

The authors declare no competing interests.

Additional information

Supplementary information The online version contains supplementary material available at https://doi.org/10.1038/s41526-024-00444-x.

Correspondence and requests for materials should be addressed to Aykut Satici or Gunes Uzer.

Reprints and permissions information is available at http://www.nature.com/reprints

Publisher's note Springer Nature remains neutral with regard to jurisdictional claims in published maps and institutional affiliations.

Open Access This article is licensed under a Creative Commons Attribution-NonCommercial-NoDerivatives 4.0 International License, which permits any non-commercial use, sharing, distribution and reproduction in any medium or format, as long as you give appropriate credit to the original author(s) and the source, provide a link to the Creative Commons licence, and indicate if you modified the licensed material. You do not have permission under this licence to share adapted material derived from this article or parts of it. The images or other third party material in this article are included in the article's Creative Commons licence, unless indicated otherwise in a credit line to the material. If material is not included in the article's Creative Commons licence and your intended use is not permitted by statutory regulation or exceeds the permitted use, you will need to obtain permission directly from the copyright holder. To view a copy of this licence, visit http://creativecommons.org/licenses/by-nc-nd/4.0/.

© The Author(s) 2024